Streaming flows generated by high-frequency small-amplitude oscillations of arbitrarily shaped cylinders

Sung Kyun Kim and Armin W. Troesch
Department of Naval Architecture and Marine Engineering, The University of Michigan, Ann Arbor, Michigan 48109

(Received 17 May 1988; accepted 14 February 1989)

Small-amplitude harmonic oscillations of arbitrarily shaped cylinders are considered both experimentally and theoretically. For the theoretical model, the flow regime is separated into inner and outer regions. In the inner region, the flow is governed by the classical Stokes boundary layer equation. In the outer region, the full Navier–Stokes equation for the steady streaming flow is solved numerically by using a finite-difference method coupled with conformal mapping techniques. Numerical results of streaming, a nonlinear response to harmonic motion, show complicated flow schemes. Experimental results confirm the existence of such flows. Streaming flow around a sharp corner of a square cylinder is investigated through numerical calculation and experimental flow visualization. The absence of any vortex shedding on the time scale of the streaming flow is noted. These results suggest that in the limit of a small amplitude of oscillation, or equivalently large Strouhal numbers, sharp-edged bodies experience attached flow in the mean sense.

I. INTRODUCTION

A flow field that has both steady and unsteady components can be initiated by a cylinder harmonically oscillating with small amplitude, or equivalently by a stationary cylinder in a harmonically oscillating onset flow. That is, a forced oscillation about a zero mean produces, in the Stokes layer, an oscillatory motion that averages to a nonzero mean. The phenomenon has classically been referred to as "steady streaming." Analytically it is explained by the presence of the "organized Reynolds stress" in the unsteady Stokes layer.[1] The average or mean motion is a consequence of the nonlinear interaction of the solid body with pure oscillatory flow.

With different combinations of Reynolds number and Strouhal number, three different flow regimes are possible: a regime without any boundary layer, a regime with one boundary layer, and a regime with two boundary layers. Following the first experimental and theoretical treatments of Faraday[2] and Rayleigh,[3] both hydrodynamicists and acousticians have investigated streaming flows in the various regimes. Schlichting,[4] Holtsmark *et al.*,[5] Stuart,[6] Riley,[7] and Wang,[8] among others, derived analytic solutions by applying a boundary layer approach and/or matched asymptotic expansions. Using numerical techniques, Davidson and Riley[9] solved the boundary layer equations for high Reynolds numbers. More recently, Haddon and Riley[10] solved the full Navier–Stokes equations for a circle in a finite domain. They used an explicit finite-difference scheme valid for moderate streaming Reynolds numbers. Their calculations gave satisfactory agreement with Bertelsen's[11] experiments.

Historically, most of the streaming work concentrated on the flow associated with circular cross sections. The axisymmetric geometry of a circle allowed researchers to simplify the boundary value problem and produce solutions that otherwise were difficult to find. There are, however, noncircular bodies that are capable of generating streaming flow. These flows may be quite unlike those found in the circular cylinder case. In this work, the hydrodynamics of oscillating noncircular two-dimensional sections is investigated. The fluid is assumed to be incompressible. The Reynolds number based on the body velocity is large while the Reynolds number based upon the streaming velocity is assumed to be of order 1 or greater. Consistent with earlier theories, the leading-order unsteady outer flow is given by the unsteady velocity potential, while in the inner region, the standard laminar boundary layer assumptions are made. It is also assumed that the flow does not separate. This assumption, on the lack of separation for a body with sharp corners, is investigated in the limiting case of the infinitesimal amplitude of oscillation.

Given the above assumptions, the tangential potential velocity next to the body determines the inner region streaming flow. Conformally mapped bodies, such as Lewis[12] forms, offer convenient closed-form expressions for the unsteady tangential potential velocities and give optimal grid generations in finite-difference approximations of the Navier–Stokes equation in the outer region. Lewis forms, which are based upon a three parameter mapping, include circles, ellipses, near rectangular sections, and many shiplike shapes. In this paper, the streaming resulting from Lewis forms and from a rectangular section with sharp corners is examined. The inner region solution is found analytically and is used as a boundary condition for the numerical solution of the full Navier–Stokes equation in the outer region. This type of numerical matching yields complex flow patterns that are qualitatively confirmed by comparison with flow visualization experiments.

II. MATHEMATICAL FORMULATION

Consider a two-dimensional body oscillating with known frequency Ω and amplitude A_0 in an incompressible Newtonian fluid. Assume that the flow resulting from the unsteady body boundary condition is laminar and that separation does not take place.[13]

The traditional nondimensional numbers, which deter-

 0899-8213/89/060975-11$01.90

mine the flow characteristics, are defined as the following:

Strouhal number: $S = \Omega L/U_0 = L/A_0$,

Reynolds number: $Re = U_0 L/\nu$,

Streaming Reynolds number: $Re_s = Re/S = U_0^2/\nu\Omega$,

where L is a length dimension of a cylinder, $\Omega = 2\pi f$ is a circular frequency, and $U_0 = \Omega A_0$. Experiments indicate that streaming motion becomes significant for small amplitudes of oscillation compared with a body dimension. For most fluids with small viscosity, the product of the Reynolds and Strouhal number is much greater than one, i.e., $Re \cdot S \gg 1$. Under these conditions there exists an unsteady Stokes layer, outside of which unsteady motion vanishes exponentially. In the outer region of the Stokes layer, flow characteristics are divided into three regimes, depending on the order of magnitude of Re_s, the streaming Reynolds number.[8] For $Re_s \ll 1$, the outer region is governed by the biharmonic equation ($\nabla^4\Psi = 0$). For $Re_s \gg 1$, in addition to the Stokes boundary layer, there is another boundary layer where streaming motion decays to zero. This double layer is described by Stuart.[6] This paper will consider moderate flows characterized by $Re_s \geqslant O(1)$, where the outer region is governed by the full Navier–Stokes equation.[9]

The two-dimensional vorticity representation of the Navier–Stokes equation and the continuity equation are given below. The dependent variables are separated into steady and unsteady components (an overbar denotes the steady component and an overtilde indicates the unsteady components), or

$$\frac{\partial \omega}{\partial t} = (u\cdot\nabla)\omega = \nu\nabla^2\omega, \quad \nabla\cdot u = 0, \quad \omega = \bar{\omega} + \tilde{\omega}, \tag{1}$$

where ω is the vorticity and u is the two-dimensional velocity vector. In this paper, ψ will represent the steady component of the streamfunction. Equation (1) can be nondimensionalized, with respect to $1/\Omega$ for time, d for length, and U_0 for the unsteady velocity, or γU_0 for the steady velocity. The ratio between the steady and unsteady velocities is defined as γ. The unsteady equivalent of Eq. (1) becomes

$$\frac{\partial \tilde{\omega}}{\partial t} - \frac{\gamma}{S}(\nabla\times\bar{u}\times\tilde{\omega} + \nabla\times\tilde{u}\times\bar{\omega}) - \frac{1}{S}(\nabla\times\tilde{u}\times\tilde{\omega})_u = -\frac{1}{Re\cdot S}(\nabla\times\nabla\times\tilde{\omega}), \quad \nabla\cdot\tilde{u} = 0, \tag{2}$$

and the steady parts are

$$(\nabla\times\tilde{u}\times\tilde{\omega})_s + \gamma^2(\nabla\times\bar{u}\times\bar{\omega}) = -(\gamma/Re)(\nabla\times\nabla\times\bar{\omega}), \quad \nabla\cdot\bar{u} = 0. \tag{3}$$

A thorough analysis of the problem posed by Eqs. (2) and (3) is given in Riley,[7] Wang,[8] and Haddon and Riley.[10] For a more detailed discussion, refer to those references. Only the relevant conclusions of the theory will be repeated here. The existence of a Stokes layer of thickness of $O(Re\cdot S)^{-1/2}$ is apparent from the fact that $Re\cdot S \gg 1$ in Eq. (2). Outside this distance the unsteady vorticity decreases exponentially. In order for the diffusive and Reynolds stress terms in Eq. (3) to balance in the Stokes layer, the velocity ratio γ must equal $1/S$.[8]

In the region outside the Stokes layer, Eq. (3) becomes

$$\nabla\times\bar{u}\times\bar{\omega} = (1/Re_s)(\nabla\times\nabla\times\bar{\omega}). \tag{4}$$

From Eq. (4), the ratio of the diffusion term to the convection term is proportional to Re_s, which for the purpose of this work is assumed to be $Re_s \geqslant O(1)$.

Similar to Wang's[8] or Riley's[7] expansion for a circular cylinder for $Re_s \ll O(1)$, a perturbation scheme is now used to set up the governing equation for the inner and outer regions for $Re_s \geqslant O(1)$. A small parameter ϵ is defined as follows:

$$\epsilon = \frac{1}{S} \ll 1, \quad \frac{1}{Re} = \alpha\epsilon,$$

$$Re_s = \frac{Re}{S} = \frac{1}{\alpha}, \quad \text{where } \alpha = O(1).$$

In a straightforward manner, the streamfunction and vorticity can be expressed in an asymptotic expansion of successive orders of ϵ. The unsteady component, through the second order, is potential flow. It includes the displacement effects of the Stokes layer but does not satisfy the no-slip condition. A stretching coordinate in the normal direction is introduced to cover boundary layer behavior.

The result in the inner region is the generalized unsteady Stokes problem of flow over an oscillating curved surface. The effect of the body shape is found indirectly in the variable pressure gradient. Specifically, the first-order steady streaming solution expressed as streamfunction $\bar{\Psi}_0$ is

$$\bar{\Psi}_0 = u_p \frac{du_p}{d\xi}\left(\frac{13}{8} - \frac{3}{4}\eta - \frac{1}{8}e^{-2\eta} - e^{-\eta}\sin\eta - \frac{3}{2}e^{-\eta}\cos\eta - \frac{1}{2}\eta e^{-\eta}\sin\eta\right), \tag{5}$$

where (η,ξ) are the local inner region normal and tangential coordinates and $u_p(\xi)e^{i\Omega t}$ is the potential flow resulting from harmonic oscillation. As $\eta \to \infty$ there is a mean motion of

$$u_s \sim -\frac{3}{4}u_p(\xi)\frac{du_p(\xi)}{d\xi}. \tag{6}$$

This becomes the steady inner boundary condition for the steady outer region in the sense of numerical matching. For a finite domain, $1 < r < \Delta$, Eq. (6) becomes, as shown in Haddon and Riley,[10]

$$u_s \sim -\frac{3\Delta^4}{4(\Delta^2-1)^2}u_p\frac{du_p}{d\xi}, \quad \text{at the inner cylinder } (r = 1)$$

and (7)

$$u_s \sim -\frac{3}{4\Delta(\Delta^2-1)^2}u_p\frac{du_p}{d\xi}, \quad \text{at the outer cylinder } (r = \Delta).$$

Consider the characteristics of this solution set represented by Eqs. (6) and (7). These solutions, which will be used as the matching condition for the outer boundary value problem, are separable into normal and tangential coordinates. The dependency in the tangential coordinate is only a function of the potential pressure gradients in a tangential direction. This fact suggests the use of conformal mapping in order to expand the results for the circular cylinder to arbi-

trary bodies. In the next section, transformations of both the governing equations and boundary conditions, based on this idea, are formulated.

From (4), the streaming in the outer region is governed by the full Navier–Stokes equation. Haddon and Riley[10] solved this equation for an oscillating circular cylinder in a finite domain using an explicit finite-difference scheme. This paper uses a similar procedure expanded to include noncircular shapes.

The outer flow is driven by the boundary conditions given in Eqs. (6) and (7), which are only dependent upon the potential pressure gradient in the tangential direction evaluated on the boundary surface. Conformal mapping offers not only a convenient method for the analytical determination of these potential flow quantities, but also provides an optimal grid generation near sharp corners. Around corners, finer meshes are expected to cover larger changes in vorticity and pressure gradients in both the normal and tangential directions. Conformal mapping automatically transforms uniform mesh in the computational circular domain into finer mesh near corners in the physical domain.

The nomenclature used to define the mapping functionals and variables are shown below in Fig. 1, where $z = f(\zeta) = X + iY$, $\zeta = e^{i\theta}$, and $\Theta = \pi/2 - \theta + \arg[f'(\zeta)]$.

There, a circle in the computational plane is mapped into the desired arbitrary shape in the physical plane. In this paper the Lewis transformation[12] for a series of rounded square cylinders, the transformation for a square cylinder,[14] and a three-parameter mapping for an asymmetric body are employed.

(1) Lewis transformation

$$z = f(\zeta) = [1/(1+b)](\zeta + b/\zeta^3). \tag{8}$$

Body shapes that correspond to $b = 0$, -0.04, -0.06, -0.08, -0.10, -0.12, and the rounded square used in the flow visualization experiment (solid line) are depicted in Fig. 2.

(2) Transformation for a square[14]

$$z = Q\left(\zeta + \sum_{m=1}^{L} \frac{a_{4m-1}}{\zeta^{4m-1}}\right), \quad \zeta = re^{i\theta}, \tag{9}$$

and

$$\frac{dz}{d\zeta} = \left[Q\left(1 + \frac{1}{\zeta^4}\right)\right]^{1/2},$$

where L is a number of truncation and

$Q = 1.180\,340\,6$,

$$a_{4m-1} = (-1)^m[(1\cdot 3\cdot 5\cdot \cdots |2m-3|)/2^m m!(4m-1)].$$

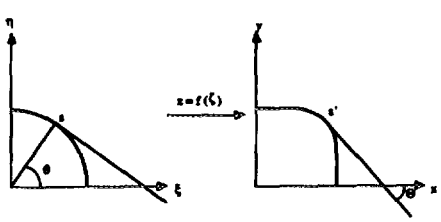

FIG. 1. The nomenclature for the conformal mapping of a circle into an arbitrary shape.

Since the mapping functionals are the form $z = C_1\zeta + C_2\zeta^{-3} + O(\zeta^{-4})$, where C is some constant, both the outer boundaries in the physical and computational planes are essentially circular in shape. In this work, the ratio of the representative cylinder dimension to the outer boundary diameter is approximately 1:26. This has the effect of reducing the second term in the mapping functional to $O(10^{-5})$ on the outer enclosure. The expression for the tangential velocities on arbitrary body boundaries is given by (A1) in the Appendix.

Bodies with sharp corners, such as a square cylinder produce flows around edges, which are difficult to analyze. The assumption of nonseparating mean flow must be examined. From the flow visualization experimental results shown in Sec. IV the following observations are made: (i) there exists no visible separation around corners in the mean sense (4 sec exposure photograph); (ii) the flow around a corner is similar to that of a stream incident upon a 45° wedge; and (iii) a trajectory of a fluid particle around a corner does not cross the corner; instead the particle forms a thin elliptic orbit that lies between the body and the 45° symmetry line. The nonzero mean of this orbital motion moves in from the symmetry line and leaves along the body surface.

Also from the theoretical and experimental works on the estimation of force components on an oscillatory cylinder by Graham[15] and Bearman *et al.*,[16] it follows that (i) the length scale in the size of vortices and shedding is proportional to the amplitude of oscillation, 1/S, (ii) the bigger S is, the more shedding processes take place in one cycle, (iii) at the larger S, diffusion of vortices into each other, i.e., equal magnitude and opposite signed pair vortices, is so rapid that little or no convection of the vortex pair was seen, and (iv) the effect of the onset of vortex shedding becomes significant at a small but finite amplitude of oscillation.

Following these observations in the limiting case of $S \to \infty$, the mean motion can be analyzed with the assumption of nonseparating flow. The only difficulty remaining in the analysis of a square is the singular behavior of the surface potential velocity at a corner. This singularity, however, can be excluded by introducing the locally valid Stokes flow around a sharp corner.[17,18] A detailed investigation of the multiscaled viscous regions is beyond the scope of this paper. Rather, the effort is focused on the necessary potential pressure gradient assumptions required for the approximate streaming flow description.

A simple model for the flow around a corner is one composed of three flow regimes, as shown in Fig. 3(a): the locally valid Stokes region (I), the unsteady boundary layer (II), and a potential flow regime (III). For small r, the behavior

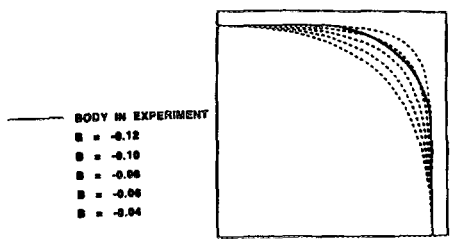

FIG. 2. The bodies generated by the Lewis transformation.

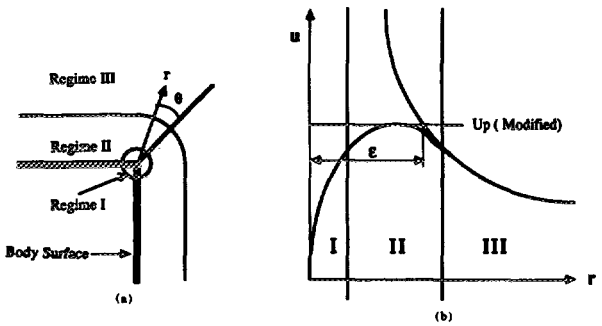

FIG. 3. The corner flow details. (a) Flow regimes near a corner (stretching the normal coordinate). (b) The characteristics of the unsteady velocity at each regime.

of the velocity near a corner is depicted in Fig. 3(b), where $u \sim r^{0.544\,48}$ in regime I and $u_p \sim r^{-1/2}$ in regime III. In the intermediate boundary layer region, the two velocities are matched. The location of maximum potential velocity, in Fig. 3(b), is represented by the point that is ϵ from the body surface (corner).

We assume that the potential velocity is equivalent to that on a body surface generated by the transformation, Eq. (9), with $r = 1 + \epsilon$. Body shapes and corresponding potential pressure gradients are depicted for some values of ϵ in Fig. 4. This assumption allows us to consider potential flows that are noninfinite at the corner.

III. NUMERICAL SOLUTION PROCEDURE

In numerical analysis, it is possible to solve an elliptic partial differential equation for a steady-state problem by solving an equivalent unsteady problem, parabolized in time. Given an initial solution, the parabolic equations are marched in time until a steady-state solution is attained. For the streaming problem described in this work, the initial solution corresponds to $\mathrm{Re}_s = 0$, for which there exists an

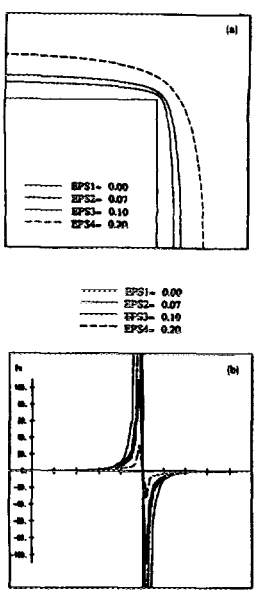

FIG. 4. The approximate modeling of the corner flow. (a) The bodies generated by the transformation shown in Eq. (9). (b) The potential pressure gradients for bodies in (a).

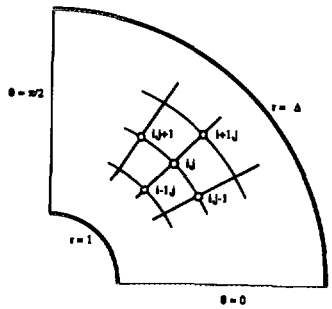

FIG. 5. The conformally mapped numerical system.

analytic solution. After the solution for a given streaming Reynolds number stabilizes, the parameter, Re_s in Eq. (4), is incremented and the time-stepping scheme repeated. While the solution technique is based upon numerical considerations, it also resembles the flow visualization experiments where the amplitude of the mechanical oscillator was increased by small increments, allowing for sufficient time between amplitude changes, so the streamlines could reach a steady-state condition.

As a result of the symmetry of flow, consider a quarter domain, as shown in Fig. 5, where $i = 1,\ldots,M+1$ and $j = 1,\ldots,N+1$. Then, define increments in r and θ as

$$\delta r = (\Delta - 1)/M \quad \text{and} \quad \delta\theta = \pi/2N.$$

The numerical formulation for the outer flow is given as

$$\frac{1}{\mathrm{Re}_s}\nabla^2\omega - \frac{1}{r}\frac{\partial(\psi,\omega)}{\partial(r,\theta)} = \frac{1}{H^2(r,\theta)}\frac{\partial\omega}{\partial t} \tag{10}$$

and

$$\nabla^2\psi = -\omega/H^2(r,\theta), \tag{11}$$

where the transformation function (the inverse of a Jacobian of the transformation) is

$$\frac{1}{H^2(r,\theta)} = \left|\frac{dz}{d\zeta}\right|^2 = J(r,\theta).$$

Equations (10) and (11) are the conformal transformations of the Navier–Stokes equation and the Poisson equation. The boundary conditions are

$$\psi = 0, \quad \text{on } r = 1,\Delta, \quad \text{for } 0<\theta<\pi/2$$

and

$$\psi = 0, \quad \text{on } \theta = 0,\pi/2, \quad \text{for } 1<r<\Delta.$$

From symmetry the vorticity has values of

$$\omega = 0, \quad \text{on } \theta = 0,\pi/2, \quad \text{for } 1<r<\Delta.$$

From the matching condition, Eq. (7), the tangential velocity becomes

$$\frac{\partial\psi}{\partial r} = u_s, \quad \text{on } r = 1,\Delta, \quad \text{for } 0<\theta<\pi/2.$$

Specifying the boundary conditions for vorticity on the body surface is one of the main difficulties when using a vorticity representation of the Navier–Stokes equation. There are many ways to represent the numerical boundary conditions. In this paper, a formula that is second-order accurate in δr is adopted.

The results at the inner cylinder, $r = 1$, are

$$\omega_{1,j} = -\frac{12[\Psi_{2,j} + (u_s^{(1)}/2)dr(2 - dr + 2\,dr^2) + (dr^2/12)(4\omega_{2,j}/H_{2,j}^2 - \omega_{3,j}/H_{3,j}^2)]H_{1,j}^2}{dr^2(3 - 2\,dr)} + O(dr^2)$$

and at the outer cylinder $r = \Delta$,

$$\omega_{M+1,j} = -\frac{12\{\Psi_{M,j} + (u_s^{(2)}/2)dr[2 - dr/\Delta + 2(dr^2/\Delta^2)] + (dr^2/12)(4\omega_{M,j}/H_{m,j}^2 - \omega_{M-1,j}/H_{M-1,j}^2)\}H_{M+1,j}^2}{dr^2[3 - 2(dr/\Delta)]},$$

where $\Psi_{i,j}^n$ denotes a point value of ψ at $r = i\delta r$, $\theta = j\delta\theta$, and $t = n\delta t$. Further, $u_s^{(1)}$ and $u_s^{(2)}$ are the matching velocities at the inner and outer cylinders, respectively.

Take the solution of Eq. (10) at $\mathrm{Re}_s = 0$; i.e., the solution to $\nabla^4\psi^0 = 0$, as the initial steady state. The biharmonic equation can be solved to give

$$\psi^0(r,\theta) = \frac{3}{8\Delta(\Delta^2 - 1)^4} u_p \frac{du_p}{d\theta}\left(B_1 r^2 + B_2 r^4 + \frac{B_3}{r^2} + B_4\right), \tag{12}$$

where

$$B_1 = 2\Delta^6 + \Delta^4 + \Delta^2 + 2, \quad B_2 = -(\Delta^4 + 1)$$
$$B_3 = \Delta^2(\Delta^6 + 1), \quad B_4 = -(\Delta^8 + 2\Delta^6 + 2\Delta^2 + 1),$$

and u_p is the potential velocity on the cylinder in an infinite domain. Equation (12) was derived through the use of the separation of variables. The algebraic programming system REDUCE[19] greatly aided in the determination of the coefficient matrix leading to Eq. (12).

For the second Re_s increment, Eq. (10) can then be solved by an explicit finite-difference scheme while Eq. (11) is solved by a generalized cycle reduction algorithm. The number of divisions in the θ direction, N, must be $2^{N_1}3^{N_2}5^{N_3}$, where N_1, N_2, and N_3 are integers. Refer to Sweet[20] for details of this algorithm. This process is repeated with successive Re_s increments until the desired Re_s is reached. Consult Haddon and Riley[10] and Telionis[1] for a discussion of this technique.

The effectiveness of the explicit scheme is limited by stability considerations. A significant reduction in the computing effort can be achieved by using the alternating direction implicit (ADI) scheme. The streamfunction is updated by using the generalized cycle reduction algorithm per each half-time step. This can be done also by using the ADI scheme of the parabolized Poisson equation per full time step.

Numerical solution procedures and brief stability analyses for both schemes are considered in the following.

A. Explicit finite-difference scheme

The following is an outline of the numerical method of Haddon and Riley.[10] Starting from the initial solution, Eq. (12), the numerical solution at $\mathrm{Re}_s = 10$ was calculated, via the partially converged solutions at $\mathrm{Re}_s = 2$ and 5. For $\mathrm{Re}_s = O(1)$, the solutions never really reached a steady state in finite time (creeping flow). These partially convergent solutions, though, were adequate as initial conditions for the next increment of Re_s. Thereafter the solution was obtained in increments of $\Delta\mathrm{Re}_s = 20$ up to $\mathrm{Re}_s = 90$. The time taken to advance the solution from one steady state to another was typically $O(10^2)$ in this range of values of Re_s. For $\mathrm{Re}_s = O(1)$, the time for a partially converged solution was taken so that body boundary values of $\partial\omega/\partial t$ were $O(10^{-4})$. Despite the simplicity of the explicit scheme, its effectiveness is limited by stability considerations. Approximate stability criteria for this scheme are

diffusion time step:

$$(\Delta t)_d \leqslant \frac{\mathrm{Re}_s}{2(1/\Delta r^2 + 1/r\,\Delta r + 1/r^2\,\Delta\theta^2)},$$

convection time step:

$$(\Delta t)_c \leqslant \frac{1}{|u_r|/\Delta r + |u_\theta|/(r\,\Delta\theta)},$$

and the actual nondimensional time step is

$$\Delta t \leqslant [1/(\Delta t)_d + 1/(\Delta t)_c]^{-1}. \tag{13}$$

Since the maximum velocity of the fluid in the annulus is less than 1.5 from Eq. (7) for a circular cylinder and for the mesh size employed here, $\Delta r = 0.109\,26$ and $\Delta\theta = 0.052\,36$; the maximum Δt available for this calculation is $O(10^{-2})$ for $\mathrm{Re}_s = O(10)$ and $O(10^{-3})$ for $\mathrm{Re}_s = O(1)$. The criterion for convergence to a steady state is based on the maximum value of $\partial\omega/\partial t$ in the flow at each time step and $O(10^{-4})$ was found to be adequate.

B. Alternating direction implicit scheme

It is difficult to obtain the exact stability criteria for an ADI approximation of the nonlinear Navier–Stokes equation. However, since the ADI scheme is second-order accurate in time and, for the heat equation, it is unconditionally stable, the time increments of this problem can be approximated by the convection time $(\Delta t)_c$, which is much larger than the time increment of Eq. (13). Moreover, the ADI scheme provides a strong numerical damping, which effectively removes short period disturbances resulting from incorrect initial conditions. These disturbances adversely affect the numerical solution in the early time stage. However, this damping is so strong that it results in an overdamped solution. Therefore a combination of the ADI and the explicit schemes is expected to obtain an accurate solution with still a far smaller computing time. The strong numerical damping and large time increment of the ADI scheme enable us to exclude all intermediate solutions in Re_s of the explicit scheme with the expense of only $O(10^2)$ time steps at $\mathrm{Re}_s = 90$. Using this damped solution as a new initial condition, the explicit finite-difference scheme is applied as before. A large saving in computing time was achieved.

IV. FLOW VISUALIZATION EXPERIMENTS

Flow visualization experiments were conducted in the Ship Hydrodynamics Laboratory at The University of Michigan. Three different techniques using hydrogen

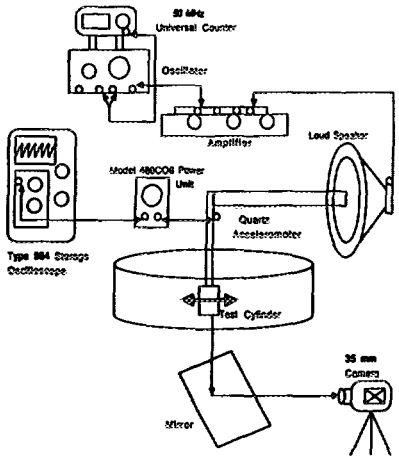

FIG. 6. The experimental setup for flow visualization photographs.

bubbles, fluorescent particles, and glass microcarrier beads (SoloHill Engineering, Inc., Ann Arbor, Michigan) as tracers were tried. The experimental setup consisted of a large circular dish, mechanical oscillator, and a 35 mm camera. A general schematic of the equipment layout is given in Fig. 6.

Harmonic oscillations were achieved by attaching the specimen to a 38.1 cm musical instrument speaker. The usable frequency range of the speaker was between 20 and 400 Hz. Test specimens had representative dimensions (diameter for the circular section or width for the rounded square and square sections) of 2.54 cm and a depth of approximately 3.8 cm. An outer boundary was created by a dish of 66.0 cm. This produced a ratio of body width to dish diameter of approximately 1:26. The sinusoidal input signal to the speaker was created by a sine wave generator and monitored by a separate frequency counter. The amplitude and frequency of oscillation were measured by a quartz accelerometer (model No. 392A, PCB Piezotronics, Inc., Depew, New York) and the output was recorded on an oscilloscope.

Initial tests with hydrogen bubbles proved unsatisfactory. The relatively small streaming velocities were affected by the velocities caused by bubble buoyancy. A more successful approach was to sprinkle fluorescent powder on the water surface and follow the particle paths under ultraviolet light. This approach, however, was suspect as a result of the presence of capillary waves. In order to eliminate the possible free surface effects, a glass cover was placed over the fluid and glass microcarrier beads were floated in a water–glycerin mixture. To make the mixture, water was carefully poured over glycerin resulting in a water–glycerin interface. The mixture was then allowed to rest for 24 h, producing a gradual density gradient varying from nearly pure glycerin on the bottom to nearly pure water at the top. The glass beads are available with a specific gravity of 1.02, 1.03, or 1.04 and a diameter range of 90–150 μm. Various combinations of water–glycerin and bead weight were tried. The best results were achieved when the beads had a specific gravity of 1.03.

In a typical test run, the test specimen would start oscillating from rest. The wave generator frequency would be set and the gain increased in increments. Sufficient time, usually 3–5 min, would be allowed between gain changes for the flow to reach steady state. When the desired streaming Reynolds number and Strouhal number were reached, a time lapsed photograph was taken. Typical exposure times were two to four seconds. Some of the resulting stream patterns are shown in Figs. 7–9, where both the fluorescent powder and the glass microcarrier beads results are presented. The streaming Reynolds numbers given in the figure captions are based upon a kinematic viscosity of $\nu = 1.35$ cm^2/sec for the water–glycerin mixture (several samples of the mixture in the interface where the beads floated were taken, and the viscosity was measured by a viscometer and averaged ten times per sample) and $\nu = 0.015$ cm^2/sec for pure water. In the water–glycerin mixture, there was a certain amount of fluid stratification at the interface where the beads were located. Visual inspection indicated that the effect of this was small on the overall flow patterns. In spite of a large change in viscosity, but a relatively small change in the density, the persistence of two-dimensionality could be seen in the experiments. Generally, the patterns were repeatable with both the fluorescent powder and glass microcarrier beads, if care was taken. The flow, however, also exhibited marked regions of instability, particularly if the apparatus was not aligned properly.

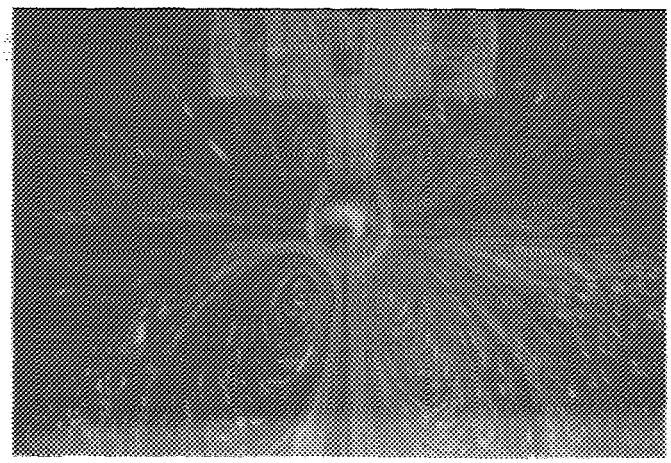

(a)

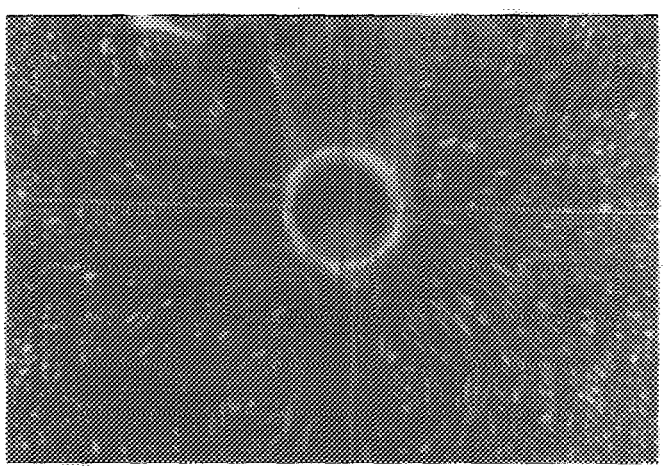

(b)

FIG. 7. The streaming flow around a circle. (a) The streaming flow on the free surface; $\mathrm{Re}_s \geqslant 50$, $S \approx 30$. (b) The streaming flow on the interface of water and glycerin; $\mathrm{Re}_s = 50$, $S = 30$.

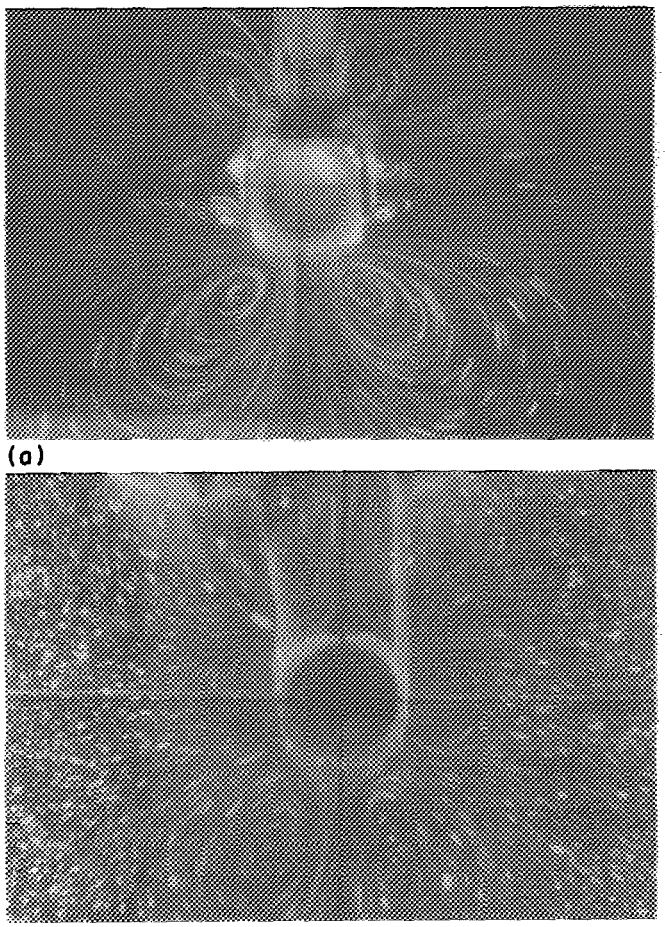

FIG. 8. The streaming flow around a rounded square. (a) The streaming flow on the free surface of water; $Re_s > 30$, $S \approx 50$. (b) The streaming flow on the interface of water and glycerin; $Re_s = 30$, $S = 50$.

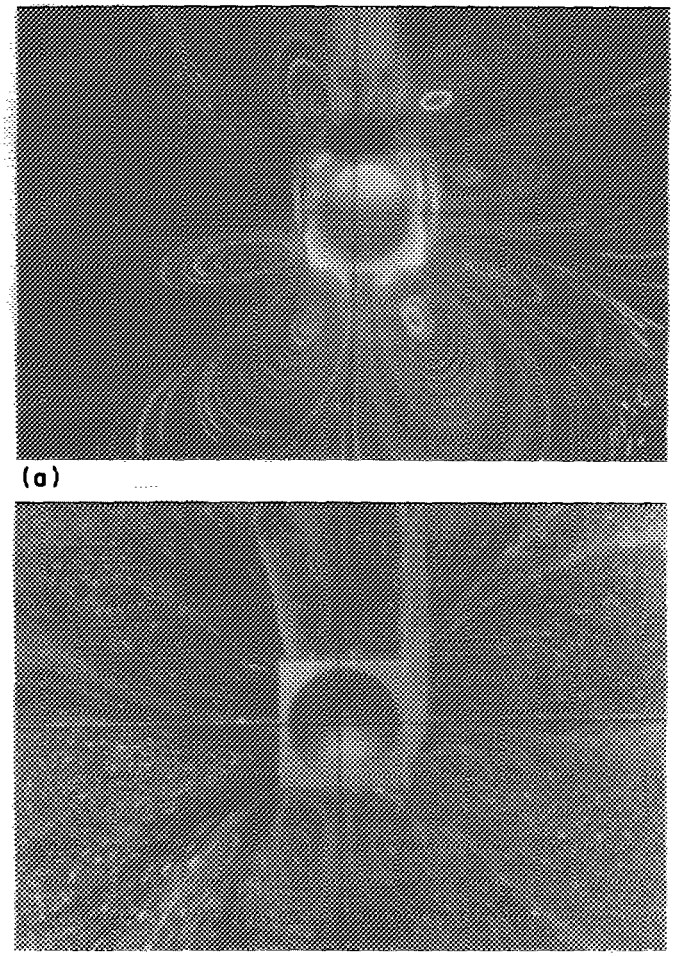

FIG. 9. The streaming flow around a square. (a) The streaming flow on the free surface of water; $Re_s > = 10$, $S \approx 100$. (b) The streaming flow on the interface of water and glycerin; $Re_s = 10$, $S = 100$.

V. RESULTS AND DISCUSSION

A. Circular cylinder

Trial runs to check the numerical solution technique were performed for a circular cylinder with $\Delta = 20.67$ and $Re_s = 90$. This is the case Haddon and Riley[10] solved numerically and Bertelsen[11] investigated experimentally. Satisfactory comparisons with the previously published results were obtained by using both numerical schemes with $N = 30$ and $M = 180$. The center of the recirculating region is at $r_c = 12.14$ and $\theta_c = 33°$, which compares well with the measured values of $r_c = 12.2$ and $\theta_c = 34°$, taken from the flow visualization photographs of Bertelsen[11] and the values of $r_c = 12.2$ and $\theta_c = 32.9°$, resulting from the numerical solution of Haddon and Riley.[10]

Streamlines at $Re_s = 90$ are depicted in Fig. 10(d) with its inner solution [Fig. 10(a)], reduced grid generation [Fig. 10(b)], and initial solution [Fig. 10(c)]. The experimental results at $Re_s = 50$ are shown in Figs. 7(a) and 6(b). Since Re·S for the experiment is much greater than $O(1)$, the inner cells are compressed next to the body and cannot be seen in the photographs.

B. Rounded square cylinder

A second set of shapes varying from nearly circular sections to rounded square sections was also investigated. The sections are mathematically represented by the Lewis transformation, given in Eq. (8). A value of $b = 0$ corresponds to a circle, while a value of $b = -0.13$ corresponds to a nearly square shape. The section contours for various values of b

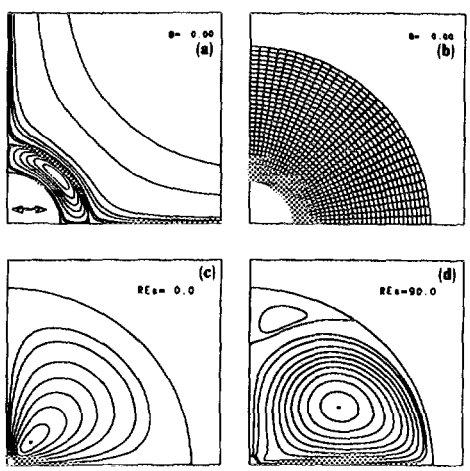

FIG. 10. The numerical solution of outer streaming flow for a circular cylinder. (a) The inner solution for a circle with $b = 0$. (b) Grid generation for the outer solution. (c) The initial condition of the outer solution; $Re_s = 0$. (d) The outer solution at $Re_s = 90$.

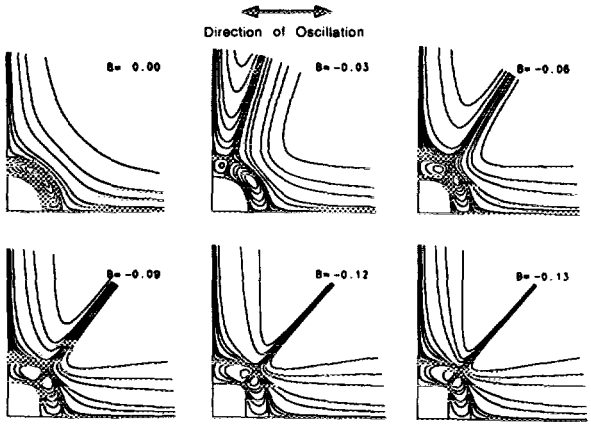

FIG. 11. Inner flows for bodies generated by the Lewis transformation.

are shown in Fig. 2. Inner solutions for the bodies of Fig. 2 are depicted in Fig. 11. A value of $b = -0.13$ is the limit for Lewis forms whose contours do not exceed the square boundary, based on the maximum width. This shape, with small radii of curvature, most closely represents a square with rounded corners.

For comparison with the rounded square used in the flow visualization experiments, the outer flow for a Lewis form of $b = -0.13$ was calculated. As shown in Fig. 2, the experimental and numerical shapes have small differences in geometry. The inner flow patterns shown in Fig. 11, however, indicate that streaming inner flows are quite similar when values of b are more negative than -0.09. Since a finer mesh size in the θ direction is expected from the inner solution, the actual number of angular and radial increments used in the simulation were $N = 60$ and $M = 180$, respectively. The initial solution for the first value of Reynolds number, $\mathrm{Re}_s = 0$, is shown in Fig. 12(c). The streamlines for the final $\mathrm{Re}_s = 30$ are then shown in Fig. 12(d). In the

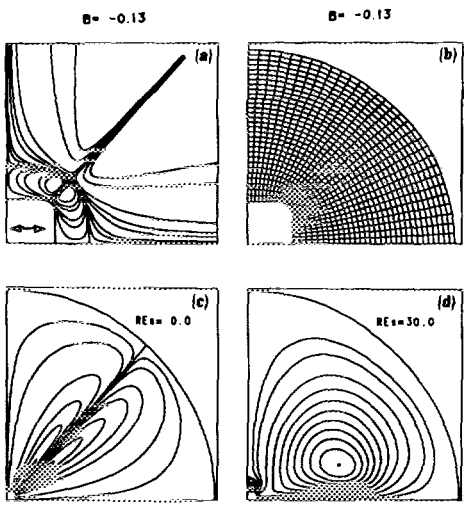

FIG. 12. The numerical solution of the outer streaming flow for a Lewis form cylinder. (a) The inner solution for a rounded square with $b = 0.13$. (b) Grid generation for the outer solution around a corner. (c) The initial condition of the outer solution; $\mathrm{Re}_s = 0$. (d) The outer solution at $\mathrm{Re}_s = 30$.

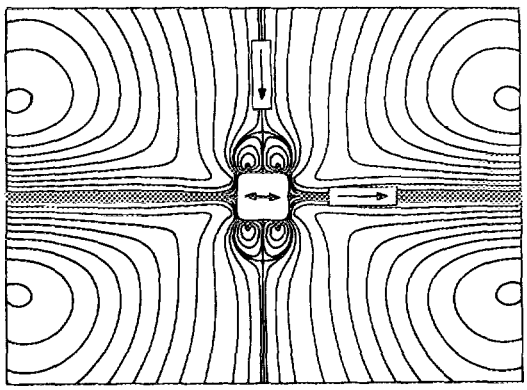

FIG. 13. The outer solution of streaming flow near a Lewis form cylinder.

limit of zero streaming Reynolds number, the outer flow pattern resembles the far field behavior of the inner solutions shown in Fig. 12(a). That is, the outer region is divided into two approximately equal recirculating cells. As the streaming Reynolds number increases, the convection terms in Eq. (10) become more important and one recirculating region shrinks to a small cell while the other grows to cover most of the outer domain. Experimental results of the streaming patterns for the rounded square at $\mathrm{Re}_s = 30$ are shown in Figs. 8(a) and 8(b). Time lapsed photographs of fluorescent particles on the free surface and glass microcarrier beads on the water–glycerin interface are given. Figure 13 shows an expanded view of the calculated streaming flow around a rounded square. Comparing Fig. 13 to Figs. 8(a) and 8(b), it is evident that there is qualitative agreement between theory and experiment. The general flow characteristics predicted by theory, four large cells in the direction of oscillation and four small cells on sides perpendicular to the direction of motion, are present in the experiments. The grid generation, as shown in Fig. 12(b), having a finer mesh around corners where the values of ψ and ω vary rapidly, is expected to produce better accuracy and convergence.

C. Square cylinder

Another obvious shape of interest is the square, since flows associated with sharp corners provide some of the more challenging problems in hydrodynamics. With the assumption on the potential pressure gradient given before, the numerical solution at $\mathrm{Re}_s = 10.0$ is solved with $\epsilon = 0.07$ (see Fig. 4).

The inner flow patterns for the square, the grid generation, the initial solution for $\mathrm{Re}_s = 0.0$, and the final outer solution, are shown in Figs. 14(a)–14(d), respectively. A magnification of the outer solution near the square boundary is shown in Fig. 15. Experimental results of streaming patterns for the square are shown in Figs. 9(a) and 9(b). Comparing Figs. 9 and 15, it is clear that there is a qualitative agreement between theory and experiment.

D. Nonsymmetric cylinder

In another application of the solution technique, the streaming of fore and aft asymmetric bodies were computed.

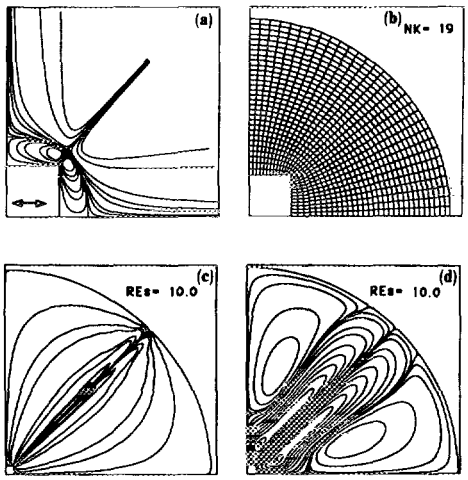

FIG. 14. The numerical solution of the outer streaming flow for a square cylinder. (a) The inner solution for a square with $LK = 20$. (b) Grid generation for the outer solution around the corner. (c) The initial condition of the outer solution; $\mathrm{Re}_s = 0$. (d) The outer solution at $\mathrm{Re}_s = 10$.

The bodies were generated by the three-term conformal mapping of

$$z = \frac{1}{1+a+b}\left(\zeta + \frac{a}{\zeta^2} + \frac{b}{\zeta^3}\right),$$

where the two cases of $a = 0.06$, $b = 0.0$ (body I) and $a = 0.03$, $b = -0.1$ (body II) were tried. Numerical solutions are shown in Figs. 16 for body I at $\mathrm{Re}_s = 50$ and Fig. 17 for body II at $\mathrm{Re}_s = 30$, respectively. These shapes were not tested experimentally, though flow patterns similar to these were observed when the symmetric test specimens were mounted incorrectly.

All of the experimental flow patterns were matched in a qualitative sense with the theoretical computations. The two dissimilar experimental techniques gave similar results, thereby increasing the level of confidence in the experiments.

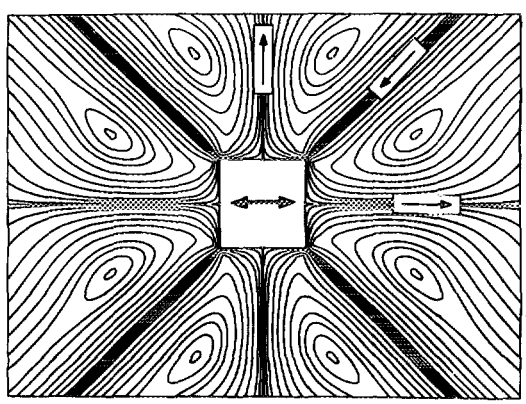

FIG. 15. The outer solution of streaming flow near a square cylinder.

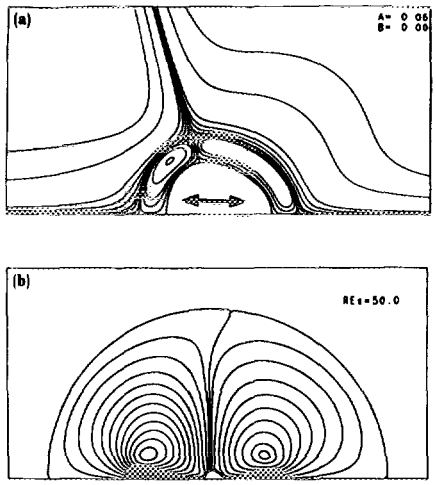

FIG. 16. The numerical solution of the outer streaming flow for an asymmetric body I. (a) The inner solution. (b) The outer solution; $\mathrm{Re}_s = 50$.

Quantitative differences were apparent, particularly in the location of the large vortex cells. Possible sources of experimental error may be the following: (i) The water–glycerin mixture was actually a stratified rather than homogeneous fluid; (ii) the rounded square did not match the exact contour of the Lewis form as shown in Fig. 2; and (iii) the fluorescent particle paths may have been influenced by the capillary waves on the free surface. These effects and the influence on streaming of the assumed pressure gradient for the square shape should be the subjects of future investigative efforts.

VI. SUMMARY

A general procedure for solving the streaming flows resulting from small amplitude oscillations of an arbitrarily shaped cylinder has been presented. The conformal mapping technique with its inherent adaptive grips, has been shown to be useful in solving the full Navier–Stokes equation for two-dimensional nonseparating flows. For the limiting case of

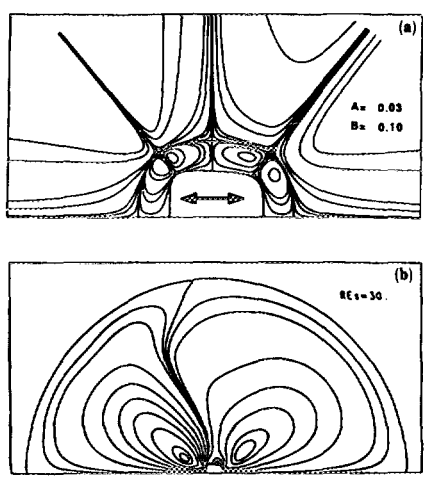

FIG. 17. The numerical solution of the outer streaming flow for an asymmetric body II. (a) The inner solution. (b) The outer solution; $\mathrm{Re}_s = 30$.

$S \to \infty$, the nonseparating model for bodies with sharp edges produces a reasonable numerical solution when compared with the experimental flow visualization results. The time-lapsed photographs clearly demonstrate that sharp cornered bodies do not experience large scale separation in the limit of large Strouhal number S.

The lack of separation on the time scale of the streaming flows indicates that the net effect of the vorticity generated at the corner is small. During each half-cycle of oscillation, a vortex is generated. This vortex is nearly equal in strength but opposite in direction to the previously generated vortex. Since there is little time for the two to separate, they combine and cancel. This is a hypothesis, however, and should be tested by additional research.

ACKNOWLEDGMENTS

This work was supported by The University of Michigan/Sea Grant/Industry Consortium in Offshore Engineering under the Michigan Sea Grant Program, projects No. E/GLE-14 and No. R/T-23, under Grant No. NA85AA-SG045C from the Office of Sea Grant, National Oceanic and Atmospheric Administration (NOAA), U.S. Department of Commerce, and funds from the State of Michigan. Industry participants include the American Bureau of Shipping; Conoco, Inc.; EXXON Production Research; Friede and Goldman, Ltd.; Nobel, Denton, and Associates, Inc.; Shell Companies Foundation (1985–1986); and the U.S. Coast Guard.

APPENDIX: THE POTENTIAL VELOCITY AND THE CORRESPONDING INNER STREAMING VELOCITY ON THE BODY SURFACE

Given the complex potential of a circle,

$$\bar{W} = U_0(\zeta + 1/\zeta).$$

Refer to Fig. 1 for the definition of the variables. Then using complex variable analysis, the tangential velocity on arbitrary bodies, $u_p(\theta)e^{i\Omega t}$, can be shown to equal

$$u_p(\theta) = \left(\frac{\partial(\mathrm{Re}\{\bar{W}\})}{\partial X(r,\theta)}\right)_{r=1}\cos\Theta + \left(\frac{\partial(\mathrm{Re}\{\bar{W}\})}{\partial Y(r,\theta)}\right)_{r=1}\sin\Theta$$

$$= \left(\frac{\partial(\mathrm{Re}\{\bar{W}\})}{r\,\partial\theta}\right)_{r=1} \times \left(-\frac{Y_r}{J}\cos\Theta + \frac{X_r}{J}\sin\Theta\right)_{r=1},$$

where the Jacobian of the coordinate transformation is

$$J = \begin{vmatrix} X_r & (1/r)X_\theta \\ Y_r & (1/r)Y_\theta \end{vmatrix} = \left(\frac{\partial X}{\partial r}\frac{\partial Y}{r\,\partial\theta} - \frac{\partial X}{r\,\partial\theta}\frac{\partial Y}{\partial r}\right)$$

and $\mathrm{Re}\{\bar{W}\}$ represents the real part of the complex potential $\bar{W}$. Finally,

$$u_p(\theta) = (2U_0\sin\theta/J_0)(X_r\sin\Theta - Y_r\cos\Theta)_{r=1}, \tag{A1}$$

where $J_0 = J(r=1)$.

(i) For a Lewis-form cylinder,

$$J_0 = [1/(1+b)]^2[(1-3b\cos 4\theta)^2 + 3b\sin 4\theta] = (1 - 6b\cos 4\theta + 9b^2)/(1+b)^2.$$

Therefore, from (A1), the surface potential velocity is

$$u_p(\theta) = [2U_0\sin\theta(1+b)/(1-6b\cos 4\theta + 9b^2)] \times [(\cos\theta - 3b\cos 3\theta)\sin\Theta - (\sin\theta + \sin 3\theta)\cos\Theta]. \tag{A2}$$

(ii) For a square cylinder,

$$J_0 = \{Q[(1+\cos 4\theta)^2 + \sin^2 4\theta]\}^{1/2} = 2Q^{1/2}(1+\cos 4\theta)^{1/2} = 2Q^{1/2}|\cos 2\theta|$$

and

$$X_r|_{r=1} = Q\left(\cos\theta - \sum_{m=1}^{L}(4m-1) \times a_{4m-1}\cos(4m-1)\theta\right),$$

$$Y_r|_{r=1} = Q\left(\sin\theta + \sum_{m=1}^{L}(4m-1) \times a_{4m-1}\sin(4m-1)\theta\right).$$

Also, the tangential angle to body surface is

$$\Theta = \begin{cases} \pi/2, & \text{for } 0<\theta<\pi/4, \\ 0, & \text{for } \pi/4<\theta<\pi/2. \end{cases}$$

Therefore, from (A1), the surface potential velocity is

$$u_p = \frac{U_0\sin\theta\,[\cos\theta + \Sigma_{m=1}^{L}(4m-1)a_{4m-1}\cos(4m-1)\theta]}{Q^{1/2}|\cos 2\theta|}, \quad \text{for } 0<\theta<\frac{\pi}{4},$$

$$u_p = \frac{U_0\sin\theta\,[\sin\theta - \Sigma_{m=1}^{L}(4m-1)a_{4m-1}\sin(4m-1)\theta]}{Q^{1/2}|\cos 2\theta|}, \quad \text{for } \frac{\pi}{4}<\theta<\frac{\pi}{2}. \tag{A3}$$

For a finite domain $r\in[1,\Delta]$, that is, a flow resulting from an oscillating circular cylinder ($r=1$) inside a finite fluid domain surrounded by a stationary outer circular cylinder ($r=\Delta$), the potential velocity on body surface can be found by the process in Haddon and Riley,[10] and this process can be generalized for an arbitrary-shaped cylinder, as in the following:

$$(u_p)_{\text{finite}} = 1/(\Delta^2-1)(u_p)_{\text{infinite}} \quad \text{at } r=\Delta \tag{A4}$$

$$(u_p)_{\text{finite}} = \Delta^2/(\Delta^2-1)(u_p)_{\text{infinite}} \quad \text{at } r=1. \tag{A5}$$

From these results, the inner solution of streaming flow for a finite domain at $r = 1$ and $r = \Delta$, using the coordinate system fixed in the mean position of circle as $\eta \to \infty$, is

$$u_s = \left(\frac{\partial \bar{\psi}}{\partial r}\right)_{r=1} = -\frac{3\Delta^4}{4(\Delta^2-1)^2} u_p(\theta) \frac{du_p(\theta)}{d\theta}, \quad \text{(A6)}$$

$$u_s = \left(\frac{\partial \bar{\psi}}{\partial r}\right)_{r=\Delta} = -\frac{3}{4\Delta(\Delta^2-1)^2} u_p(\theta) \frac{du_p(\theta)}{d\theta}. \quad \text{(A7)}$$

Here (A6) and (A7) are used as a matching condition for the outer streaming problem.

[1]D. P. Telionis, *Unsteady Viscous Flows* (Springer, Berlin, 1981), p. 154.
[2]M. Faraday, Philos. Trans. R. Soc. London **121**, 299 (1831).
[3]L. Rayleigh, Philos. Trans. R. Soc. London **175**, 1 (1883); Sci. Pap. **2**, 239 (1883).
[4]H. Schlichting, Phys. Z. **3**, 327 (1932).
[5]J. Holtzmark, I. Johnsen, T. Sikkeland, and S. Skavlem, J. Acoust. Soc. Am. **26**, 26 (1954).
[6]J. T. Stuart, Fluid Mech. **24**, 274 (1966).
[7]N. Riley, Math. **12**, 161 (1965).
[8]C. Y. Wang, Fluid Mech. **32**, 55 (1968).
[9]B. J. Davidson and N. Riley, Fluid Mech. **53**, 287 (1972).
[10]E. W. Haddon and N. Riley, Q. J. Mech. Appl. Math. **32**, 263 (1979).
[11]A. F. Bertelson, Fluid Mech. **64**, 579 (1974).
[12]F. M. Lewis, Soc. Nav. Archit. Mar. Eng. Trans. **37**, 1 (1929).
[13]G. K. Batchelor, *Fluid Dynamics* (Cambridge U.P., London, 1973), p. 353.
[14]L. Landweber, Ship Res. **23**, 3 (1979).
[15]J. M. R. Graham, Fluid Mech. **97**, 331 (1980).
[16]P. W. Bearman, M. J. Downie, J. M. R. Graham, and E. D. Obasaju, Fluid Mech. **154**, 337 (1985).
[17]H. J. Lugt and E. W. Schwiderski, Proc. R. Soc. London Ser. A **185**, 382 (1965).
[18]U. Ghia and R. T. Davis, AIAA J. **12**, 1659 (1974).
[19]*REDUCE User's Manual*, edited by A. C. Hearn (Rand Corporation, Santa Monica, CA, 1985), Sec. 3.2.
[20]R. A. Sweet, SIAM J. Numer. Anal. **11**, 3, 506 (1974).